Article

Trends of Pd₃Au(111) Alloy Surface Segregation in Oxygen, Carbon, and Nitrogen Environments

Published as part of The Journal of Physical Chemistry C virtual special issue "Jens K. Nørskov Festschrift".

Olga V. Vinogradova, Karsten Reuter, and Vanessa J. Bukas*

Cite This: *J. Phys. Chem. C* 2023, 127, 22060−22066

Read Online

ACCESS | Metrics & More | Article Recommendations | SI Supporting Information

ABSTRACT: Catalytic properties of alloys are largely determined by the specific chemical composition at the surface. Differences in composition between surface and bulk regions depend intricately on both the parent metals and the surrounding environment. While a nonreactive environment favors surface segregation of the more noble alloy component, a reactive environment such as oxygen is expected to draw the more active component to the surface. Using *ab initio* thermodynamics, we explore here the structure and composition of the Pd₃Au(111) alloy surface in oxygen, carbon, and nitrogen containing environments with reference to, *e.g.*, gas phase O_2, CH_4, and N_2 reservoirs, respectively. An extensive and systematic search of the available phase-space shows the segregation profile in an oxygen atmosphere following the anticipated picture described above, with O preferentially staying at the surface. In contrast, carbon at low coverages burrows deeper into the alloy substrate without a significant effect on the segregation profile. A nitrogen environment induces an intermediate behavior to oxygen and carbon, where the nitrogen atoms first favor either surface or subsurface sites depending on the detailed metallic composition profile. Our results overall demonstrate the complex response that has to be expected for an active alloy surface during catalysis while assessing the level of detail that is required to be accounted for in corresponding reaction models.
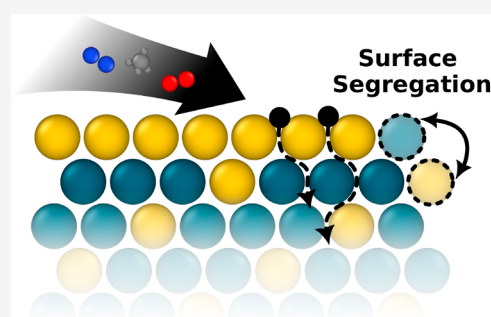
1. INTRODUCTION

Operating catalysts are dynamic in nature and can undergo even dramatic structural and compositional changes under realistic reaction conditions.[1,2] In the case of alloy catalysts, in particular, the composition of the relevant (catalytically) active phase may be entirely different from that of the ordered bulk as certain species preferentially segregate at the surface. Surface segregation is driven by intrinsic differences in reactivity between the different alloy components as, for example, one (or more) of the metals are more strongly "pulled" from the bulk to form stable surface or near-surface phases with reactive species of the environment. The resulting operando surface composition is critical to the function and performance of the alloy as demonstrated numerous times, *e.g.*, in both cases of heterogeneous thermal and electro-catalysis.[3−5] Furthermore, the presence of subsurface species and impurities tends to change the surface chemistry.[6,7] And yet, operando insight into the dynamic evolution of alloy catalysts is generally limited and remains an open challenge in catalysis research.

As *in situ* characterization techniques for probing the catalyst surface are maturing,[8,9] first-principles theory is challenged by the vast phase space that must be explored when searching for thermodynamically stable alloy configurations in a reactive environment. As a simple working example, we note the early 2008 study by Kitchin *et al.* which investigated Ag₃Pd(111) surface segregation in an oxygen atmosphere.[10] This study

considered varying metal composition "only" in the uppermost two surface layers, while restricting atomic O adsorption to "only" one of the four fcc on-surface sites of a periodic (2×2) unit cell. Already this simple problem added up to a total of 375 surface slab calculations. While this may still be considered manageable with an efficient electronic structure method like density functional theory (DFT) and modern-day computational resources, the problem at hand becomes much more complex if modeling a larger unit cell or additional adsorption/intercalation sites. As a result, it is generally unclear how sensitive the surface segregation profile is to changes in the bulk alloy composition or to different operating environments.
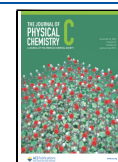
In order to establish a deeper trend understanding, we investigate here segregation at a Pd₃Au(111) alloy surface in oxygen-, carbon-, and nitrogen containing environments. While keeping focus on general trends rather than a particular application, the choice of the Pd−Au model catalyst system is motivated by its relevance for many chemical transformations

including coupling,[11] pollution control,[12] dehydrogenation,[13] and oxidation reactions.[14,15] We first develop a systematic approach based on *ab initio* thermodynamics to explore the available phase space while including nonstoichiometric compositions of the Pd and Au component metals, as well as surface and subsurface intercalation sites for the external environment species. In the next step, we construct and compare surface free energy diagrams under varying operation conditions. This analysis reveals a trend of surface segregation that is consistent with the reactivity of intercalated species across the periodic table: oxygen prefers to bind at the surface, and this drives segregation of the more active Pd alloy component, while likely also signaling the onset of bulk oxidation. The smaller carbon atoms, on the other hand, seek higher coordination and therefore burrow deeper into the alloy bulk while occupying interstitial lattice sites and leaving the more noble Au component at the surface. Finally, nitrogen shows an intermediate behavior compared to oxygen and carbon, where the occupation of surface or subsurface sites depends upon the detailed alloy composition. Our results overall demonstrate the complex response that can be expected for an active alloy surface during real catalysis, while highlighting the importance of accounting for alloy non-stoichiometries as well as subsurface chemistry in corresponding DFT models.

2. METHODS

2.1. Surface Free Energy. We investigated the alloy surface segregation profile by developing a computational framework based on *ab initio* thermodynamics. The underlying methodology has previously been described in detail for clean metal surfaces,[16,17] oxide surfaces,[18−20] and alloys.[10] In the following, we summarize this methodology as presented by Kitchin *et al.* for a Pd−Ag alloy surface in an oxygen environment[10] and adapt it to our current problem. Specifically, we consider here a Pd−Au alloy surface with a larger search space, *i.e.*, more adsorption/intercalation sites, and generalize the equations below for any type of external (*e.g.*, oxygen, carbon, and nitrogen) species from the environment.

We start by assuming that the Pd−Au alloy surface is in equilibrium both with a bulk Pd_3Au phase and with the gas-phase environment of species i. These systems act as thermodynamic reservoirs that can exchange particles with the surface: the Pd_3Au bulk provides Pd and Au atoms of chemical potential μ_{Pd} and μ_{Au} respectively, while the surrounding environment provides particles i (here $i = \{O, C, N\}$ atoms) of chemical potential μ_i. A general equation for the surface free energy γ can then be written as

$$\gamma(T, p_{gas}, N_i, N_{slab}, x_{Pd}, x_{Au}) =$$

$$\frac{1}{2A}[G_{slab}(T, p_{gas}, N_i, N_{slab}, x_{Pd}, x_{Au}) - N_{slab}x_{Pd}\mu_{Pd}$$
$$- N_{slab}x_{Au}\mu_{Au} - N_i\mu_i(T, p_{gas})] \tag{1}$$

where G_{slab} is the free energy of the surface slab that can be estimated using DFT (*cf.* Sections 2.3 and 2.4). Conditions (T, p_{gas}) correspond to the (constant) temperature and gas phase pressure respectively, and thus also determine μ_i. While the above expression is currently formulated in a way that suggests a gas-phase reference, it is important to note that the general

framework works for any type of reservoir that is in thermodynamic equilibrium and exchanges species of chemical potential μ_i with the slab (such as, *e.g.*, the solid, bulk phases used later). The term N_i is the number of adsorbed/intercalated species i within the slab, while N_{slab} is the total number of metal (Pd + Au) slab atoms. Mole fractions x_{Pd} and x_{Au} represent the ratios of Pd and Au within the slab, so that $x_{Pd} + x_{Au} = 1$. Finally, A is the surface area of the slab and the factor of 2 accounts for a symmetric slab model as used in all following DFT simulations (*cf.* Section 2.2).

The chemical potentials μ_{Pd} and μ_{Au} are not independent from one another, but related through the bulk alloy chemical potential μ_{bulk}, *i.e.*, the Gibbs free energy per atom of the bulk alloy (here Pd_3Au). By considering $\mu_{bulk} = x_{Au,bulk}\mu_{Au} + x_{Pd,bulk}\mu_{Pd}$ and the same constraint on mole fractions of the bulk ($x_{Pd,bulk} + x_{Au,bulk} = 1$), eq 1 can be simplified as

$$\gamma(T, p_{gas}, N_i, N_{slab}, x_{Pd}, x_{Au}) =$$

$$\frac{1}{2A}[G^{slab}(T, p_{gas}, N_i, N_{slab}, x_{Pd}, x_{Au}) - N_{slab}\mu_{Pd_3Au,bulk}$$

$$- N_{slab}\Delta\mu_{Pd-Au}(x_{Pd} - x_{Pd,bulk})$$
$$- N_i\mu_i(T, p_{gas})] \tag{2}$$

where $\Delta\mu_{Pd-Au} = \mu_{Pd} - \mu_{Au}$ is the Pd−Au energy difference in the bulk alloy. According to this formulation, therefore, the third term in eq 2 accounts for possible nonstoichiometric ratios of alloy components in the slab as compared to the bulk reservoir.

The term $\Delta\mu_{Pd-Au}$ will change depending on how far a nonstoichiometric surface deviates from the corresponding bulk phase. Therefore, a valid range for this term can be defined between the cases where surface segregation induces the slab to be fully Pd-covered and fully Au-covered. In a case where Pd segregates to the surface, the bulk reservoir is assumed to be rich in Pd so that it can induce that phase separation. Similarly, in the case where Au segregates to the surface, the bulk reservoir is assumed to be rich in Au. These two limits of phase separation are termed Pd-rich and Au-rich, respectively. The difference $\Delta\mu_{Pd-Au}$ of a given slab will therefore always be bound according to

$$\frac{\mu_{Pd_3Au,bulk} - \mu_{Au}}{x_{Pd,bulk}} \leq \Delta\mu_{Pd-Au} \leq \frac{\mu_{Pd} - \mu_{Pd_3Au,bulk}}{x_{Au,bulk}} \tag{3}$$

where the lower and upper limits represent the Au-rich and Pd-rich cases, respectively.

2.2. Structural Models. The bulk Pd_3Au alloy is modeled according to the $L1_2$ ($Pm\bar{3}m$) structure with a lattice constant of $a = 4.024$ Å as optimized using our computational setup (*cf.* Section 2.3). Surfaces are then constructed in the (111) orientation using the Atomic Simulation Environment.[21] Specifically, we use a seven-layer (2×2) symmetric supercell with a constrained middle layer while allowing all outer three layers on each side to relax. A vacuum region of at least 16 Å is chosen between slabs in the nonperiodic z direction. Bulk fcc Pd and Au were predicted with optimized lattice constants of 3.970 and 4.181 Å, respectively.

The chemical potential of environment O, C, and N species is referenced in the following either against gas-phase O_2, CH_4, or N_2 reservoirs (top x-axes in Figures 2−4) or against bulk
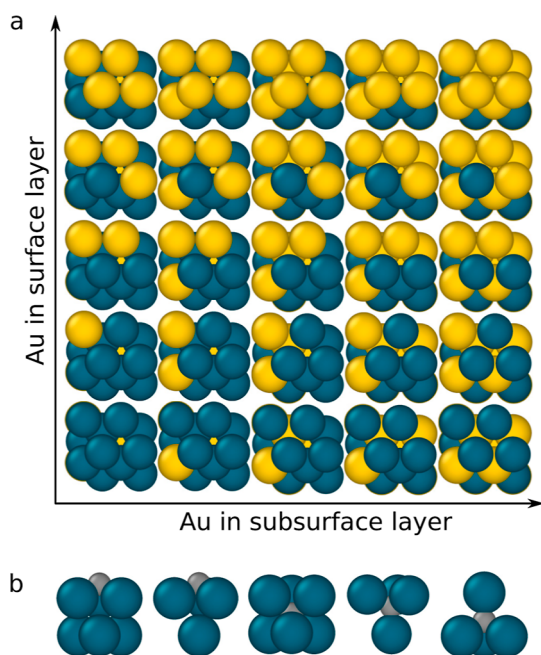
Figure 1. (a) Top views of the (2×2) surface unit-cells of all 25 unique substrate alloy slabs where Pd_3Au is used as the bulk composition and the outer two layers are varied in their Pd–Au ratio. (b) Side views illustrating the five unique adsorption sites considered in this study: surface fcc, hcp, and subsurface octahedral, and two types of tetrahedral sites (from left to right).

Figure 2. Surface free energy γ of $Pd_3Au(111)$ in an oxygen-containing environment, while in equilibrium with a (a) Pd-rich (top) and (b) Au-rich (bottom) Pd_3Au bulk reservoir. We plot γ as a function of the O chemical potential referenced to bulk PdO (bottom x-axis) or gas phase O_2 at standard conditions (top x-axis). The vertical dotted lines mark thermodynamic equilibrium with the bulk oxide. Each solid line corresponds to one of the tested surface configurations: colored lines mark minimum energy configurations of a given O content, while the thicker path outlines the overall most stable configurations within the given range of O chemical potential. These configurations are depicted in the insets (top and side views) with Pd atoms colored teal, Au in gold, and O in red.

Pd-based oxide, carbide, or nitride structures (bottom x-axes in Figures 2–4). These bulk reference structures are taken from the Materials Project[22] database as those with the lowest formation energy; *cf.* Supporting Information, Section S3 for further details.

2.3. Computational Details. All DFT calculations are performed with the Quantum Espresso[23,24] (version 6.6) software package and the revised Perdew–Burke–Ernzerhof (RPBE) exchange–correlation functional.[25] Calculations do not include spin-polarization. A plane wave basis set describes the electronic states with energy cutoff values of 540 eV for surface slabs and 680 eV for bulk structures and gas phase molecules. Brillouin zone sampling uses Fermi–Dirac smearing (0.05 eV width) along with a $20 \times 20 \times 20$ Monkhorst–Pack k-point grid[26] for calculations of all bulk reference structures, $8 \times 8 \times 1$ grid for surface slabs, and simple Γ-point for gas phase molecules. Dipole corrections were applied to all surface calculations. Finally, we use the Broyden–Fletcher–Goldfarb–Shanno (BFGS) algorithm for geometry relaxations with a convergence criteria of ≤ 0.05 eV/Å for atomic forces and ≤ 0.005 eV for the total energy.

2.4. Free Energy Contributions. Free energy contributions are considered on top of the total DFT-calculated energies (E_{total}) in order to arrive at surface free energy γ according to eq 2. For this purpose, it is important to note that this relation relies on *differences* of Gibbs free energy such that we can expect a large degree of cancellation, especially between free energy contributions of the solid surface and bulk. We therefore make the approximation $G \approx E_{total}$ for the surface and bulk systems, neglecting pressure–volume and entropic contributions, based on the detailed formalism described in refs 10, 16, and 20. A ballpark estimate on the configurational entropy contribution for the present system (<14.5 meV/Å² at 300 K) is included in Supporting Information, Section S7. For
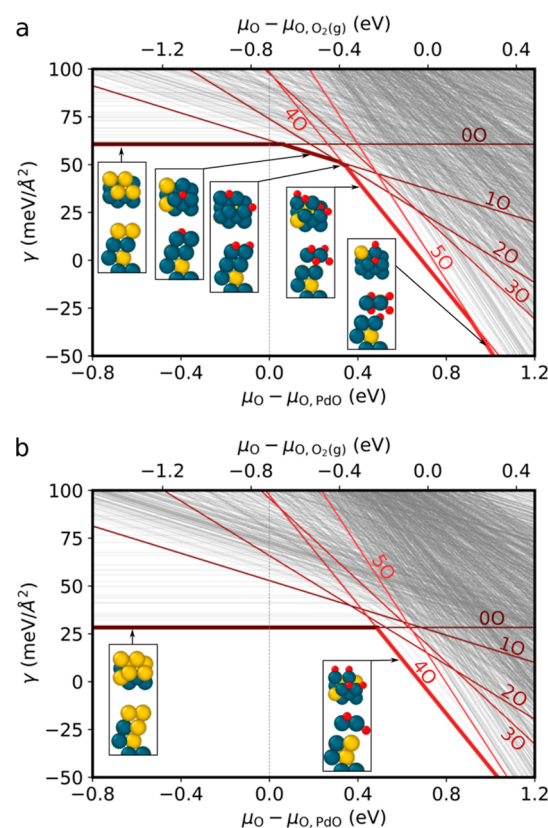
gas phase CH_4 ($+H_2$) and N_2 reference molecules, we include contributions from zero point energy as well as entropic contributions at given (T, p_{gas}) conditions in the ideal gas approximation (Supporting Information, Section S2). On the other hand, the chemical potential of gas phase O_2 was directly approximated from the experimental H_2O formation free energy[27] in order to avoid the well-known overbinding error produced by semilocal DFT[28] (Supporting Information, Section S2).

3. RESULTS AND DISCUSSION

3.1. Defining the Search Space. We first construct a structural database to sample the configurational space of nonstoichiometric Pd–Au substrates with adsorbed/intercalated species from the surrounding environment. This database accounts for varying alloy composition within the two outer surface layers on each side of our symmetric slab model, while the middle three layers maintain bulk Pd_3Au stoichiometry. Systematically exchanging the eight metal atoms at the surface and subsurface of our (2×2) surface unit cell results in 25 unique substrate geometries, ranging from all Au atoms to all Pd atoms, as shown in Figure 1a. Single O, C, or N species are
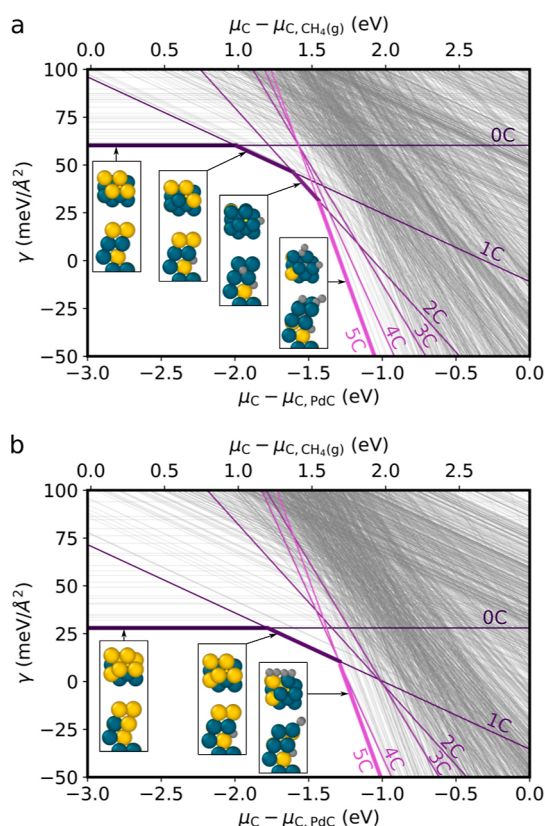
Figure 3. Surface free energy γ of $Pd_3Au(111)$ in a carbon-containing environment, while in equilibrium with a (a) Pd-rich (top) and (b) Au-rich (bottom) Pd_3Au bulk reservoir. We plot γ as a function of the C chemical potential referenced to bulk PdC (bottom x-axis) or gas phase CH_4 at standard conditions (top x-axis). Each line corresponds to one of the tested surface configurations: colored lines mark minimum energy configurations of a given C content, while the thicker path outlines the overall most stable configurations within the given range of C chemical potential. These configurations are depicted in the insets (top and side views) with Pd atoms colored teal, Au atoms colored gold, and C in purple.

Figure 4. Surface free energy γ of $Pd_3Au(111)$ in a nitrogen-containing environment, while in equilibrium with a (a) Pd-rich (top) and (b) Au-rich (bottom) Pd_3Au bulk reservoir. We plot γ as a function of the N chemical potential referenced to bulk Pd_3N (bottom x-axis) or gas phase N_2 at standard conditions (top x-axis). The vertical dotted lines mark the thermodynamic equilibrium with the bulk nitride. Each solid line corresponds to one of the tested surface configurations: colored lines mark minimum energy configurations of a given N content, while the thicker path outlines the overall most stable configurations within the given range of N chemical potential. These configurations are depicted in the insets (top and side views), with Pd atoms in teal, Au in gold, and N in blue.

then placed either directly at the surface or within the first two interstitial layers (while keeping the slab inversely symmetric): fcc and hcp adsorption sites are considered at the surface, while octahedral and two distinct types of tetrahedral sites sample the subsurface (*cf.* Figure 1b). This gives a total count of 32 possible sites (8 on the surface and 12 in each of the first and second interstitial layers) that can be occupied by an external atom within each of the 25 substrates of Figure 1a. We depict the full set of these 32 sites in Figure S1 of the Supporting Information.

It is clear from the sample size of 25 substrate geometries and up to 32 adsorption sites that our search space grows rapidly, to the point of being unmanageable, with an increasing number of adsorbed/intercalated atoms from the environment. As a quick estimate: if we do not take care to remove duplicate structures, 800 configurations must be evaluated when considering the addition of a single external atom on all substrates and within all sites. Expanding to two added atoms in a next step would therefore require the evaluation of 12,400 configurations within a naive brute force approach. Already this search space is prohibitively large for exploration with DFT, even with modern computational resources. We therefore follow instead a reductionist approach where each nth atom
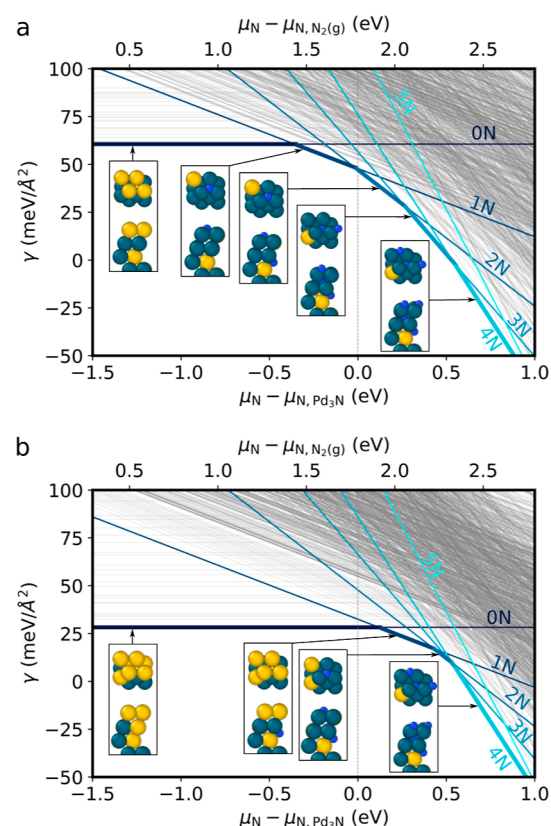
added uses as starting structure only the minimum-energy ($n-1$)-atom configuration for a given alloy substrate. In practice, this means that from the set of 800 single-adsorbate configurations, we select the 25 most stable configurations for each of the unique substrates of Figure 1a and these configurations are used as a basis for adding a second atom in all unoccupied sites. This creates a set of 775 double-adsorbate configurations, from which another 25 minimum-energy configurations are selected, and so on. We sequentially expand our database in this way, up until five external species are adsorbed/intercalated within our slab model. Along the way, high-energy structures and duplicates are avoided by rejecting configurations where the surface reconstructs or where an adsorbate moves from one adsorption site to more than halfway toward a neighboring one (defined here as a distance >1.5 Å). This filtering ensures faster convergence to the most stable configurations within our search space.

3.2. Oxygen-Induced $Pd_3Au(111)$ Surface Segregation. Following the above methodology, we start our analysis with $Pd_3Au(111)$ surface segregation in an oxygen-containing environment. Figure 2 shows the predicted surface free energy γ as a function of the O chemical potential μ_O while in

equilibrium with either a Pd-rich (top) or Au-rich (bottom) Pd_3Au bulk reservoir. Each gray line shown corresponds to an independent DFT calculation as we explore the emerging phase space of 1893 inequivalent surface configurations in this case (after reducing and filtering as described in Section 3.1). We use colored lines, however, to mark those configurations that are detected as most stable for a given O content and highlight in bold the overall path of lowest energy. The results in Figure 2 generally follow the anticipated trend: at the lower μ_O, i.e., under O-poor environmental conditions, the clean surface structures are favored and Au is exposed at the surface as the more noble of the two alloy components. This preference is not surprising given the significantly lower Au(111) surface free energy of 38 meV/Å^2 when compared to the corresponding 85 meV/Å^2 for Pd(111). As oxygen adsorbs at a higher μ_O, it drives segregation of the more active Pd alloy component to the surface. This effect occurs at higher μ_O, i.e., a more reactive/aggressive oxygen environment, in the Au-rich as compared to the Pd-rich reservoir limit. This is all consistent with the trend reported by Kitchin et al. for O-induced segregation at $Ag_3Pd(111)$.[10] And yet, as compared to that study, we find a different sequence of stable surface configurations with increasing oxygen reactivity. We identify the reason behind this difference as the inclusion of subsurface intercalation sites within our study.

At low coverages, oxygen prefers to bind at fcc sites on the surface with the highest possible coordination to neighboring Pd atoms. For the case of a Pd-rich environment, Figure 2a specifically shows up to two surface O atoms favorably adsorbed this way in our (2×2) model unit cell. Beyond this 0.5 ML coverage, however, we predict the formation of a stable oxide-like phase as two extra O species are added to subsurface tetrahedral sites (between the first and second outer surface layers). This oxide phase is similarly found for the case of a Au-rich environment in Figure 2b. Its formation here directly follows the clean surface though (without on-surface O adsorption) and occurs at a slightly (0.15 eV) higher μ_O as compared with the Pd-rich case, thus suggesting that the presence of Au delays oxidation.

Finally, it should be noted that both Pd-rich and Au-rich cases predict the existence of the surface oxide phase within a μ_O range, where O is more thermodynamically stable in bulk PdO ($\mu_O - \mu_{O,PdO} > 0$). As a result, it remains unclear from the present analysis whether this (metastable) surface oxide phase can exist kinetically against PdO bulk or even be detected experimentally as a (transient) first step toward Pd-oxidation.[29] Regardless of this situation, however, we must stress here again the importance of considering subsurface species' intercalation when exploring the configurational phase space. Without the inclusion of such tetrahedral intercalation sites here, for example, the oxide-like surface configuration would have been entirely missed (cf. Figure S5) to yield qualitatively different results regarding the surface alloy composition in a reactive oxygen environment.[10]

3.3. Carbon-Induced $Pd_3Au(111)$ Surface Segregation.
Unlike oxygen, carbon does not directly adsorb onto the $Pd_3Au(111)$ surface but prefers to burrow deeper into the bulk. This result clearly emerges from the surface free energy diagrams of Figure 3 which we create in this case based on a pool of 1748 unique surface configurations and following the same methodology as above. Here, both Pd-rich (top) and Au-rich (bottom) bulk reservoir limits show first C species occupying octahedral lattice sites that reside between the

second and third surface layers, i.e., the deepest interstitial sites provided by the present slab model. As a result of this deep subsurface intercalation, the surface segregation profile remains unperturbed, and the noble Au component is predominantly exposed in the outer layer. This suggests therefore a less dramatic surface response than in an oxygen-containing atmosphere during, e.g., oxidation catalysis, where already quite O-poor conditions were predicted to drive substantial adsorbate-induced segregation. Only with increasing C content at higher chemical potentials μ_C, do we start seeing on-surface C adsorption and corresponding segregation of the more active Pd component as described for the oxygen-containing environment in Section 3.2. We predict all such surface configurations as thermodynamically favored against the bulk Pd-carbide (PdC) reference considered here.

While the small simulation cells used here preclude any reasonable description of bulk C intercalation or predictions regarding C saturation, we can still draw a number of useful qualitative conclusions. First, we note that favorable C−C bonds start to form with excess carbon at the surface. Despite limiting our present analysis to only five C species, these bonds imply much higher surface C concentration in larger unit cells for the same or even lower μ_C and likely act as precursors to longer carbon chains or graphite flakes.[30] In a catalytic context, such surface configurations most likely signal the onset of coking with simultaneous poisoning or deactivation of the catalyst. Second, similar to the case of oxygen above, we find that the presence of Au tends to hinder C intercalation as well as the accumulation of excess C at the surface. Correspondingly, the depth of C intercalation changes too. In pure Pd, we predict that C remains trapped within the first interstitial layer (Supporting Information, Figure S3), in agreement with experiment[7] and previous theoretical work.[31,32] As already described above and shown in Figure 3, however, the presence of Au favors an interstitial C between the second and third surface layers. Corresponding C depth profiles tracing the minimum energy paths are computed using the machine learning accelerated nudged elastic band method (AID-NEB)[33] and are provided in Figures S6 and S7 of the Supporting Information. Differences in energy barriers for moving a carbon atom from the surface to the bulk support the depth of C intercalation in both pure Pd or PdAu. Lastly, the difference between Pd and Au lattice constants (3.970 vs 4.181 Å, cf. Supporting Information, Section S3) induces at least some amount of strain in surfaces with greater segregation. Effects of this strain are fortified by the intercalated species at higher μ_C, though the absolute results for higher concentration structures should only be viewed here as a conceptual extrapolation. In reality, the surface will likely break up into more complex structures to relieve the strain.

3.4. Nitrogen-Induced $Pd_3Au(111)$ Surface Segregation.
Lastly, we predict that nitrogen has an intermediate effect on the $Pd_3Au(111)$ surface segregation compared to oxygen and carbon. In this situation, a Pd-rich or Au-rich bulk reservoir limit makes a big difference, as seen by comparing Figure 4a and b. These surface free energy diagrams are once again constructed in the same way as before, but using a data set of 1601 unique surface configurations to sample the available phase space with N adsorption/intercalation. Focusing first on the region of lowest chemical potentials μ_N considered, we find that the location of the first added N species is sensitive to whether the model uses a Pd-rich or Au-rich assumption. In the case of excess Pd (Figure 4a), nitrogen

is most stable on the surface and induces Pd surface segregation, similar to what happens in the oxygen environment. Conversely, in the case of excess Au, nitrogen prefers to intercalate to a deeper octahedral interstitial site and thus leaves the surface with Au segregation as in the carbon environment. Furthermore, the onset of these events differ by a significant ≈ 0.5 eV in μ_N such that N is always more thermodynamically favorable within a bulk Pd-nitride (Pd$_3$N) reference structure in the Au-rich limit but not necessarily in the Pd-rich limit.

4. SUMMARY AND CONCLUSIONS

In summary, we use *ab initio* thermodynamics to explore the segregation profiles of a Pd$_3$Au(111) alloy surface in oxygen, carbon, and nitrogen environments. This systematic comparison reveals a complex dependence upon the inherent reactivity of the intercalated species. While a nonreactive environment will naturally induce surface segregation of the more noble (Au) alloy component, reactive O species favor the more active (Pd) component as they bind to the surface. Adsorption at fcc sites of the surface, along with subsurface intercalation at tetrahedral sites within the first interstitial layer, forms a stable oxide-like surface phase that likely signals the onset of catalyst oxidation. Carbon prefers higher coordination compared to oxygen, however, and therefore occupies (octahedral) lattice sites deeper within the alloy bulk. As a result, the more noble Au component remains dominant at the surface. While not captured within our small simulation cells, we predict that excess C starts accumulating only at the surface after the subsurface is saturated and that this will then ultimately lead to catalyst deactivation (in the form of coking). Lastly, nitrogen yields an intermediate response to oxygen and carbon, where the favored adsorption/intercalation sites (and therefore surface segregation profiles) depend sensitively upon the detailed metallic composition. In all cases, the presence of Au "shields" the alloy from the reactive environment, *i.e.*, requiring more aggressive conditions to initiate a reaction.

The trend among O, C, and N intercalations that emerges from our analysis is summarized in Figure 5. This figure plots the relative-to-bulk intercalation free energy as a function of intercalation depth for atomic O, C, and N species in pure Pd.
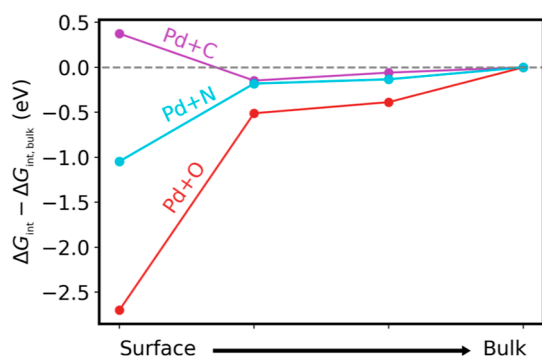

Figure 5. Intercalation free energy for the O, N, and C species at Pd, relative to the corresponding values for intercalation within bulk fcc Pd. Data from left to right indicate increasing intercalation depth from surface to bulk: on-surface adsorption, intercalation within the first interstitial layer, intercalation within the second interstitial layer, and intercalation within the bulk lattice. The first three data points use a seven-layer (2×2) Pd(111) surface slab model, while the last data point uses a bulk ($3 \times 3 \times 3$) Pd cell.

Specifically, from left to right, we consider external species being added to the surface, to the first interstitial layer, second interstitial layer, and to the bulk, respectively [for detailed surface free energy plots of Pd(111) in each environment, *cf.* Figures S2–S4]. This shows the energetic preference for surface over bulk intercalation in the case of oxygen, bulk over surface intercalation in the case of carbon, and something in between for the case of nitrogen. This result clearly demonstrates the importance of considering also subsurface phenomena in operando models of a catalyst surface.

■ ASSOCIATED CONTENT

ⓢ Supporting Information

The Supporting Information is available free of charge at https://pubs.acs.org/doi/10.1021/acs.jpcc.3c05640.

> Considered adsorption/intercalation sites; gas- and bulk-phase references; surface phase diagrams for Pd(111); and NEB analysis on the role of subsurface carbon intercalation (PDF)
>
> Optimized structures and raw energy data (ZIP)

■ AUTHOR INFORMATION

Corresponding Author

Vanessa J. Bukas − *Fritz-Haber-Institut der Max-Planck-Gesellschaft, D-14195 Berlin, Germany;* ⓞ orcid.org/0000-0002-0105-863X; Email: bukas@fhi.mpg.de

Authors

Olga V. Vinogradova − *Fritz-Haber-Institut der Max-Planck-Gesellschaft, D-14195 Berlin, Germany;* ⓞ orcid.org/0000-0001-5862-3639

Karsten Reuter − *Fritz-Haber-Institut der Max-Planck-Gesellschaft, D-14195 Berlin, Germany;* ⓞ orcid.org/0000-0001-8473-8659

Complete contact information is available at:
https://pubs.acs.org/10.1021/acs.jpcc.3c05640

■ ACKNOWLEDGMENTS

■ REFERENCES

(1) Kalz, K. F.; Kraehnert, R.; Dvoyashkin, M.; Dittmeyer, R.; Gläser, R.; Krewer, U.; Reuter, K.; Grunwaldt, J.-D. Future challenges in heterogeneous catalysis: understanding catalysts under dynamic reaction conditions. *ChemCatChem* **2017**, *9*, 17−29.

(2) Goodman, D. Model catalysts: from imagining to imaging a working surface. *J. Catal.* **2003**, *216*, 213−222.

(3) Greeley, J.; Stephens, I.; Bondarenko, A.; Johansson, T. P.; Hansen, H. A.; Jaramillo, T.; Rossmeisl, J.; Chorkendorff, I.; Nørskov,

J. K. Alloys of platinum and early transition metals as oxygen reduction electrocatalysts. *Nat. Chem.* **2009**, *1*, 552−556.

(4) Escudero-Escribano, M.; Malacrida, P.; Hansen, M. H.; Vej-Hansen, U. G.; Velazquez-Palenzuela, A.; Tripkovic, V.; Schiotz, J.; Rossmeisl, J.; Stephens, I. E.; Chorkendorff, I. Tuning the activity of Pt alloy electrocatalysts by means of the lanthanide contraction. *Science* **2016**, *352*, 73−76.

(5) Yang, B.; Burch, R.; Hardacre, C.; Headdock, G.; Hu, P. Influence of surface structures, subsurface carbon and hydrogen, and surface alloying on the activity and selectivity of acetylene hydrogenation on Pd surfaces: A density functional theory study. *J. Catal.* **2013**, *305*, 264−276.

(6) Teschner, D.; Borsodi, J.; Wootsch, A.; Révay, Z.; Hävecker, M.; Knop-Gericke, A.; Jackson, S. D.; Schlögl, R. The roles of subsurface carbon and hydrogen in palladium-catalyzed alkyne hydrogenation. *Science* **2008**, *320*, 86−89.

(7) Rose, M.; Borg, A.; Mitsui, T.; Ogletree, D.; Salmeron, M. Subsurface impurities in Pd(111) studied by scanning tunneling microscopy. *J. Chem. Phys.* **2001**, *115*, 10927−10934.

(8) Bergmann, A.; Roldan Cuenya, B. Operando insights into nanoparticle transformations during catalysis. *ACS Catal.* **2019**, *9*, 10020−10043.

(9) Plodinec, M.; Nerl, H. C.; Girgsdies, F.; Schlögl, R.; Lunkenbein, T. Insights into chemical dynamics and their impact on the reactivity of Pt nanoparticles during CO oxidation by operando TEM. *ACS Catal.* **2020**, *10*, 3183−3193.

(10) Kitchin, J. R.; Reuter, K.; Scheffler, M. Alloy surface segregation in reactive environments: first-principles atomistic thermodynamics study of Ag₃Pd(111) in oxygen atmospheres. *Phys. Rev. B: Condens. Matter Mater. Phys.* **2008**, *77*, 075437.

(11) Pérez-Temprano, M. H.; Casares, J. A.; Espinet, P. Bimetallic Catalysis using Transition and Group 11 Metals: An Emerging Tool for C-C Coupling and Other Reactions. *Chem.—Eur. J.* **2012**, *18*, 1864−1884.

(12) Nutt, M. O.; Hughes, J. B.; Wong, M. S. Designing Pd-on-Au bimetallic nanoparticle catalysts for trichloroethene hydrodechlorination. *Environ. Sci. Technol.* **2005**, *39*, 1346−1353.

(13) Han, S.; Mullins, C. B. Catalytic reactions on Pd-Au bimetallic model catalysts. *Acc. Chem. Res.* **2021**, *54*, 379−387.

(14) Enache, D. I.; Edwards, J. K.; Landon, P.; Solsona-Espriu, B.; Carley, A. F.; Herzing, A. A.; Watanabe, M.; Kiely, C. J.; Knight, D. W.; Hutchings, G. J. Solvent-free oxidation of primary alcohols to aldehydes using Au-Pd/TiO₂ catalysts. *Science* **2006**, *311*, 362−365.

(15) Yin, Y. B.; Heck, K. N.; Coonrod, C. L.; Powell, C. D.; Guo, S.; Reynolds, M. A.; Wong, M. S. PdAu-catalyzed oxidation through in situ generated H₂O₂ in simulated produced water. *Catal. Today* **2020**, *339*, 362−370.

(16) Rogal, J.; Reuter, K. Ab initio atomistic thermodynamics for surfaces: A primer. In *Experiment, Modeling and Simulation of Gas Surface Interactions for Reactive Flows in Hypersonic Flights*; Research and Technology Organization, NATO, 2007; pp 2-1−2-18.

(17) Vitos, L.; Ruban, A.; Skriver, H. L.; Kollár, J. The surface energy of metals. *Surf. Sci.* **1998**, *411*, 186−202.

(18) Opalka, D.; Scheurer, C.; Reuter, K. Ab initio thermodynamics insight into the structural evolution of working IrO₂ catalysts in proton-exchange membrane electrolyzers. *ACS Catal.* **2019**, *9*, 4944−4950.

(19) Reuter, K.; Scheffler, M. Composition and structure of the RuO₂(110) surface in an O₂ and CO environment: Implications for the catalytic formation of CO₂. *Phys. Rev. B: Condens. Matter Mater. Phys.* **2003**, *68*, 045407.

(20) Reuter, K.; Scheffler, M. Composition, structure, and stability of RuO₂(110) as a function of oxygen pressure. *Phys. Rev. B: Condens. Matter Mater. Phys.* **2001**, *65*, 035406.

(21) Hjorth Larsen, A.; Jørgen Mortensen, J.; Blomqvist, J.; Castelli, I. E.; Christensen, R.; Dułak, M.; Friis, J.; Groves, M. N.; Hammer, B.; Hargus, C.; et al. The atomic simulation environment—a Python library for working with atoms. *J. Condens. Matter Phys.* **2017**, *29*, 273002.

(22) Jain, A.; Ong, S. P.; Hautier, G.; Chen, W.; Richards, W. D.; Dacek, S.; Cholia, S.; Gunter, D.; Skinner, D.; Ceder, G.; et al. Commentary: The Materials Project: A materials genome approach to accelerating materials innovation. *APL Mater.* **2013**, *1*, 011002.

(23) Giannozzi, P.; Baroni, S.; Bonini, N.; Calandra, M.; Car, R.; Cavazzoni, C.; Ceresoli, D.; Chiarotti, G. L.; Cococcioni, M.; Dabo, I.; et al. QUANTUM ESPRESSO: a modular and open-source software project for quantum simulations of materials. *J. Phys.: Condens. Matter* **2009**, *21*, 395502.

(24) Giannozzi, P.; Andreussi, O.; Brumme, T.; Bunau, O.; Buongiorno Nardelli, M.; Calandra, M.; Car, R.; Cavazzoni, C.; Ceresoli, D.; Cococcioni, M.; et al. Advanced capabilities for materials modelling with Quantum ESPRESSO. *J. Phys.: Condens. Matter* **2017**, *29*, 465901.

(25) Hammer, B.; Hansen, L. B.; Nørskov, J. K. Improved adsorption energetics within density-functional theory using revised Perdew-Burke-Ernzerhof functionals. *Phys. Rev. B: Condens. Matter Mater. Phys.* **1999**, *59*, 7413−7421.

(26) Monkhorst, H. J.; Pack, J. D. Special points for Brillouin-zone integrations. *Phys. Rev. B: Solid State* **1976**, *13*, 5188−5192.

(27) Dean, J. A., Ed. *Lange's Handbook of Chemistry*, 15th ed.; McGraw-Hill: New York, 1999.

(28) Carbogno, C.; Groß, A.; Meyer, J.; Reuter, K. In *Dynamics of Gas-Surface Interactions: Atomic-level Understanding of Scattering Processes at Surfaces*; Díez Muiño, R., Busnengo, H. F., Eds.; Springer Berlin Heidelberg: Berlin, Heidelberg, 2013; pp 389−419.

(29) Rogal, J.; Reuter, K.; Scheffler, M. Thermodynamic stability of PdO surfaces. *Phys. Rev. B: Condens. Matter Mater. Phys.* **2004**, *69*, 075421.

(30) Guo, J.; Xu, C.; Sheng, F.; Shi, Z.; Dai, J.; Li, Z.; Hu, X. Simulation on initial growth stages of graphene on Pt(111) surface. *J. Appl. Phys.* **2012**, *111*, 044318.

(31) Gracia, L.; Calatayud, M.; Andrés, J.; Minot, C.; Salmeron, M. Migration of the subsurface C impurity in Pd(111). *Phys. Rev. B: Condens. Matter Mater. Phys.* **2005**, *71*, 033407.

(32) Studt, F.; Abild-Pedersen, F.; Bligaard, T.; Sørensen, R.; Christensen, C.; Nørskov, J. On the Role of Surface Modifications of Palladium Catalysts in the Selective Hydrogenation of Acetylene. *Angew. Chem., Int. Ed.* **2008**, *47*, 9299−9302.

(33) Garrido Torres, J. A.; Jennings, P. C.; Hansen, M. H.; Boes, J. R.; Bligaard, T. Low-scaling algorithm for nudged elastic band calculations using a surrogate machine learning model. *Phys. Rev. Lett.* **2019**, *122*, 156001.